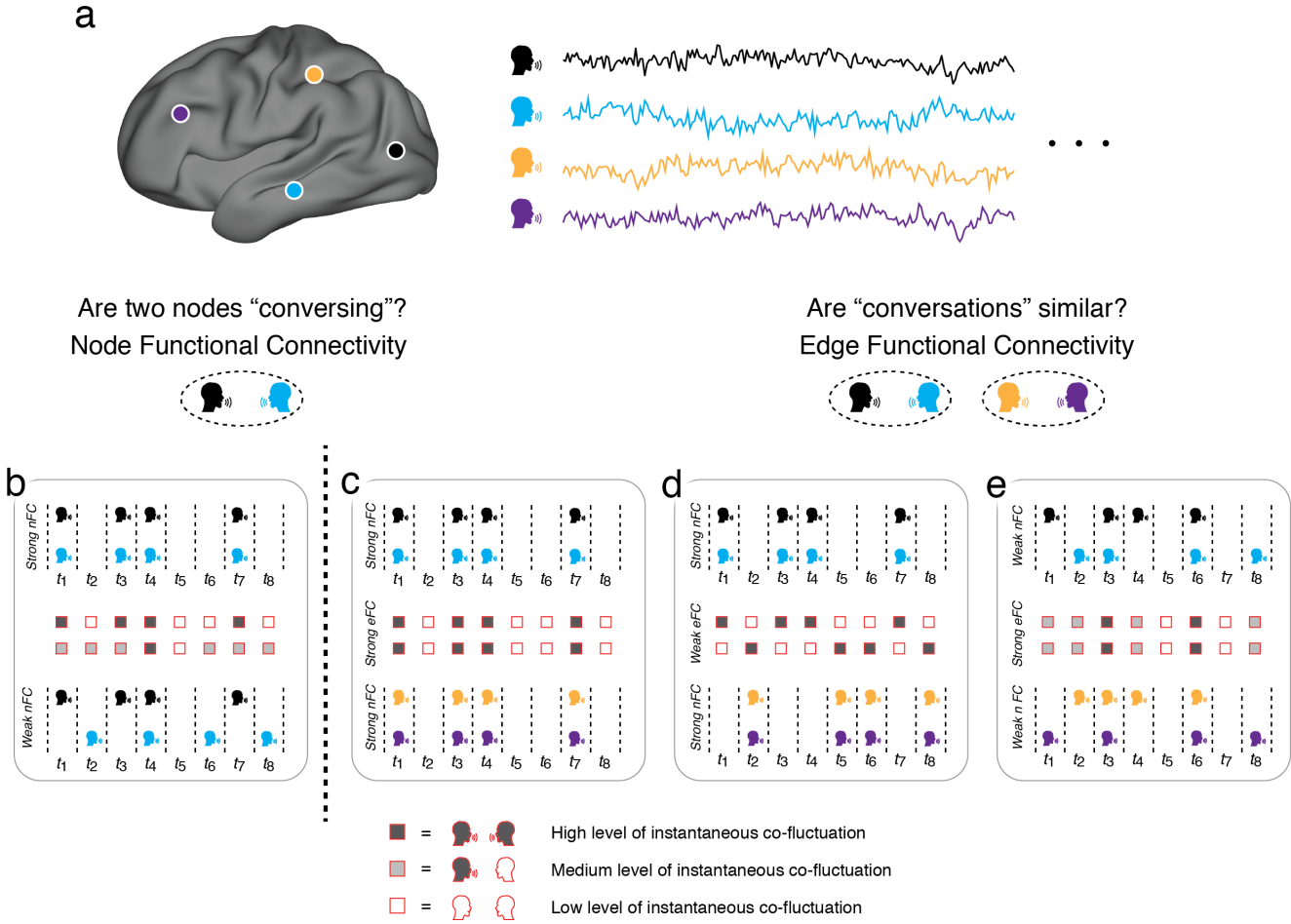


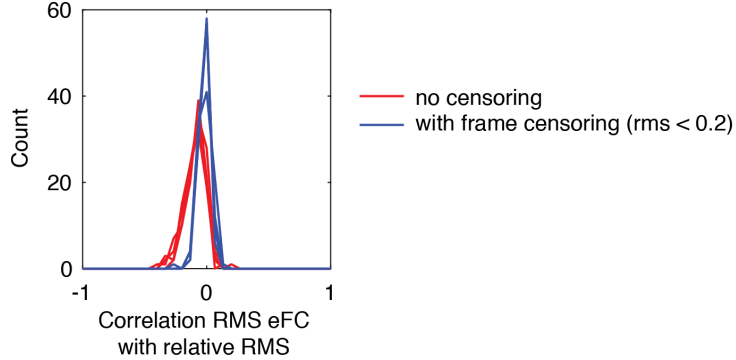
Supplementary information

Edge-centric functional network representations of human cerebral cortex reveal overlapping system-level architecture

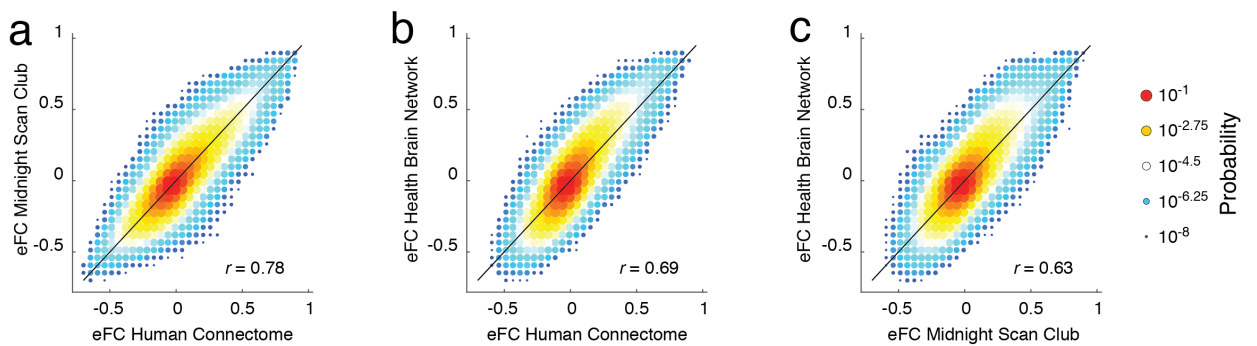
In the format provided by the
authors and unedited



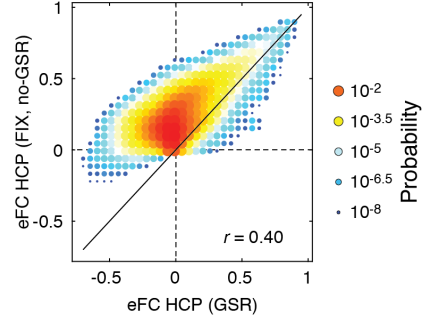
Supplementary Figure 1. An intuitive schematic of edge functional connectivity. (a) Functional connectivity measures the statistical similarity of activity recorded from pairs of neural elements (nodes). (b) Strong functional connectivity reflects temporally correlated activity (*top*), which can informally be interpreted as a measure of communication or the strength with which nodes are conversing. Conversely, weak functional connectivity (*bottom*) reflects asynchronous activity, indicating the absence of communication. The edge-centric perspective, on the other hand, tracks the conversation between two nodes across time (the shading with red boxes indicate the instantaneous magnitude of conversation; darker and lighter colors indicate strong and weak communication, respectively). These time-varying estimates – which we refer to as “edge time series” – can be related to one another through the construct of edge functional connectivity. Whereas traditional node functional connectivity measures the extent to which two nodes converse with one another on average, edge functional connectivity focuses on the dynamics of their conversation and estimates the extent to which similar conversations are taking place in the brain simultaneously. Node and edge functional connectivity are complementary to one another and emphasize unique features of brain networks. Consider the examples shown in panels *c-e*. In *c* we show a case of two functionally connected pairs of nodes whose edge time series are also correlated (see red squares between the two time series). Strong node functional connectivity, however, does not imply strong edge connectivity. In panel *d* we show, again, two functionally connected nodes whose edge times series are exactly asynchronous and whose edge connectivity would be weak. Similarly, weak node functional connectivity does not imply weak edge connectivity. In panel *e* we show examples of weakly functionally connected nodes whose edge time series are nonetheless correlated with one another. We note that this schematic serves only to provide an intuitive description of eFC and its relationship with nFC. In reality, neural time series are signed and continuously-valued; their statistical dependences are more complicated than the idealized relationships depicted in panels *b-e*.



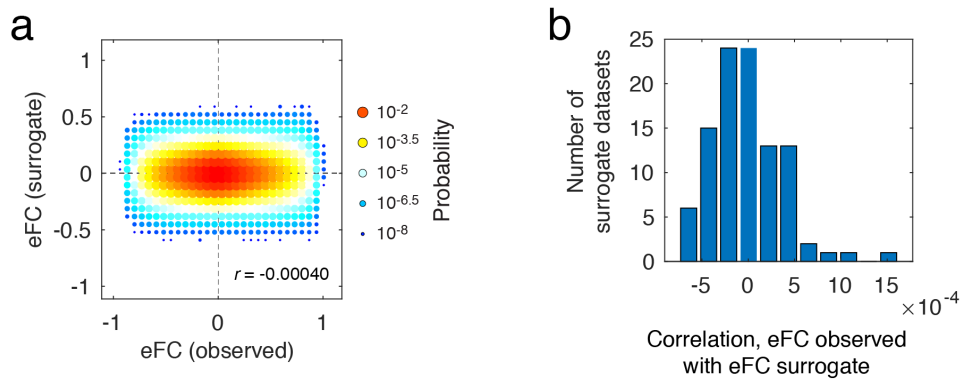
Supplementary Figure 2. Effect of in-scanner motion on co-fluctuation time series. The edge time series shown Fig. 4a is typical and consistent with what we observed in other subjects. One of the most salient features of the edge time series is their sparse temporal structure. Rather than exhibiting smooth and continuous fluctuations over time, the edge time series exhibit long periods of quietude punctuated by large “events” when many edges simultaneously exhibit large shifts in amplitude. This pattern is not unlike typical framewise displacement plots, where excessive head motion is rarely sustained over long periods of time. This raises the concern that edge time series events are simple reflections of in-scanner head motion. To address this concern, we calculated the correlation of event amplitude at each time point (RMS eFC) with the instantaneous estimates of relative motion RMS. If the events were associated with in-scanner motion, we would expect the correlation to be strong and positive. We performed this procedure for all 100 subjects in the HCP dataset and for each of the four scans, independently. We carried out two versions of this analysis. In the first (labeled “no censoring”), we retained all volumes. In the other, we excluded volumes for which motion was greater than 0.2 mm. Here, we overlay four probability distributions (histograms) of RMS-motion correlations for four scans: REST1_LR, REST1_RL, REST2_LR, and REST2_RL. We found that, in general, the correlation of edge amplitude motion was weak. Without censoring, the median correlation across all 400 HCP scans was -0.08 with an interquartile range of [-0.14, -0.03]. With censoring, this distribution was narrowed, so that the median value was still close to zero, -0.01 with interquartile ranges of [-0.05, 0.02]. Collectively, these results suggest that the observed events are likely not direct consequences of in-scanner motion.



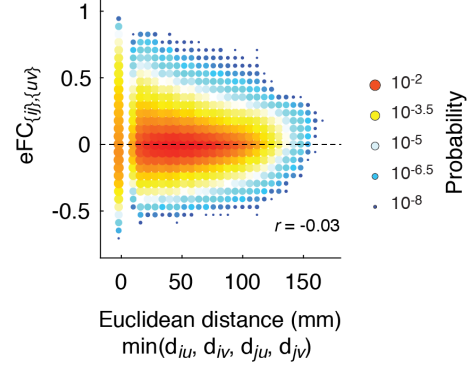
Supplementary Figure 3. Comparison of group-averaged eFC across datasets. Here, we show two-dimensional histograms comparing the similarity of group-averaged eFC matrices for each of the three datasets: Human Connectome Project, Midnight Scan Club, and the Healthy Brain Network Serial Scanning Initiative. Point size and color are proportional to probability (see key in figure).



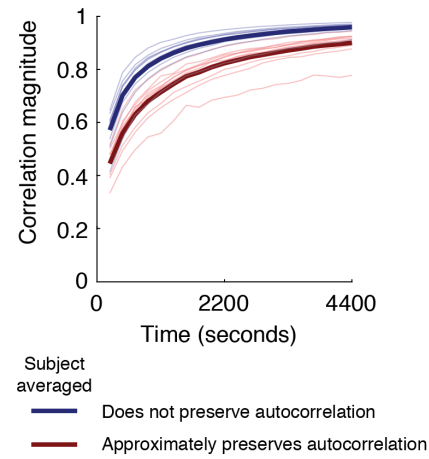
Supplementary Figure 4. Effect of global signal regression on eFC. Here, we show two-dimensional histograms comparing the similarity of group-averaged eFC from the HCP dataset preprocessed with global signal regression (36 parameter) and without (ICA-FIX). Point size and color are proportional to probability (see key in figure).



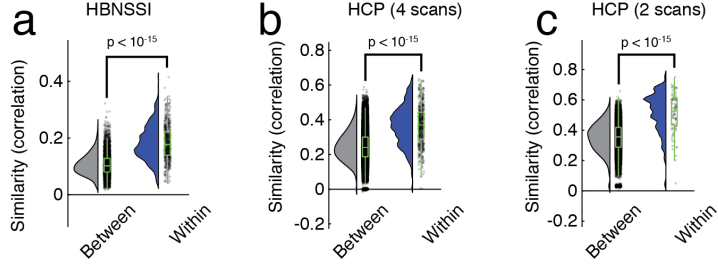
Supplementary Figure 5. Comparison of observed eFC with surrogate eFC. In the main text we analyzed eFC constructed from fMRI BOLD time series. Here, we compare the structure of that observed eFC with the eFC estimated from phase-randomized surrogate time series (random phase between $[0, 2\pi]$ added to each frequency bin uniformly across all brain regions). We show results for subject 100307 from the Human Connectome Project dataset. (a) Two-dimensional histogram of observed eFC and eFC from one surrogate run. Point size and color are proportional to probability (see key in figure). (b) Histogram of similarity (correlation) between observed and surrogate eFC connection weights across 100 independent runs of the phase-randomization procedure. Note that, in general, the observed eFC and the surrogate eFC are uncorrelated.



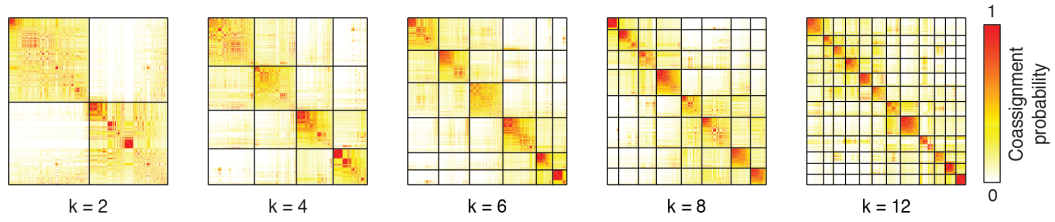
Supplementary Figure 6. Relationship of eFC with alternative distance metric. In the main text we calculated the correlation of eFC with the surface area of the quadrilateral formed by the four nodes participating in that connection, reporting a weak negative correlation. Here, we test an alternative distance metric calculated as the minimum Euclidean distance between pairs of nodes participating in the edge connection. That is, given the edges $\{i, j\}$ and $\{u, v\}$, we calculate their distance as: $D_{ij,uv} = \min(d_{iu}, d_{iv}, d_{ju}, d_{jv})$, where d_{ij} is the Euclidean distance between the centroids of nodes i and j . Unlike the surface area described in the main text, this distance metric has the property that if any node is repeated among i , j , u , and v , distance is equal to 0. As in the main text, we find that this alternative distance metric does not explain variation in eFC weights ($r = -0.03$). Point size and color are proportional to probability (see key in figure).



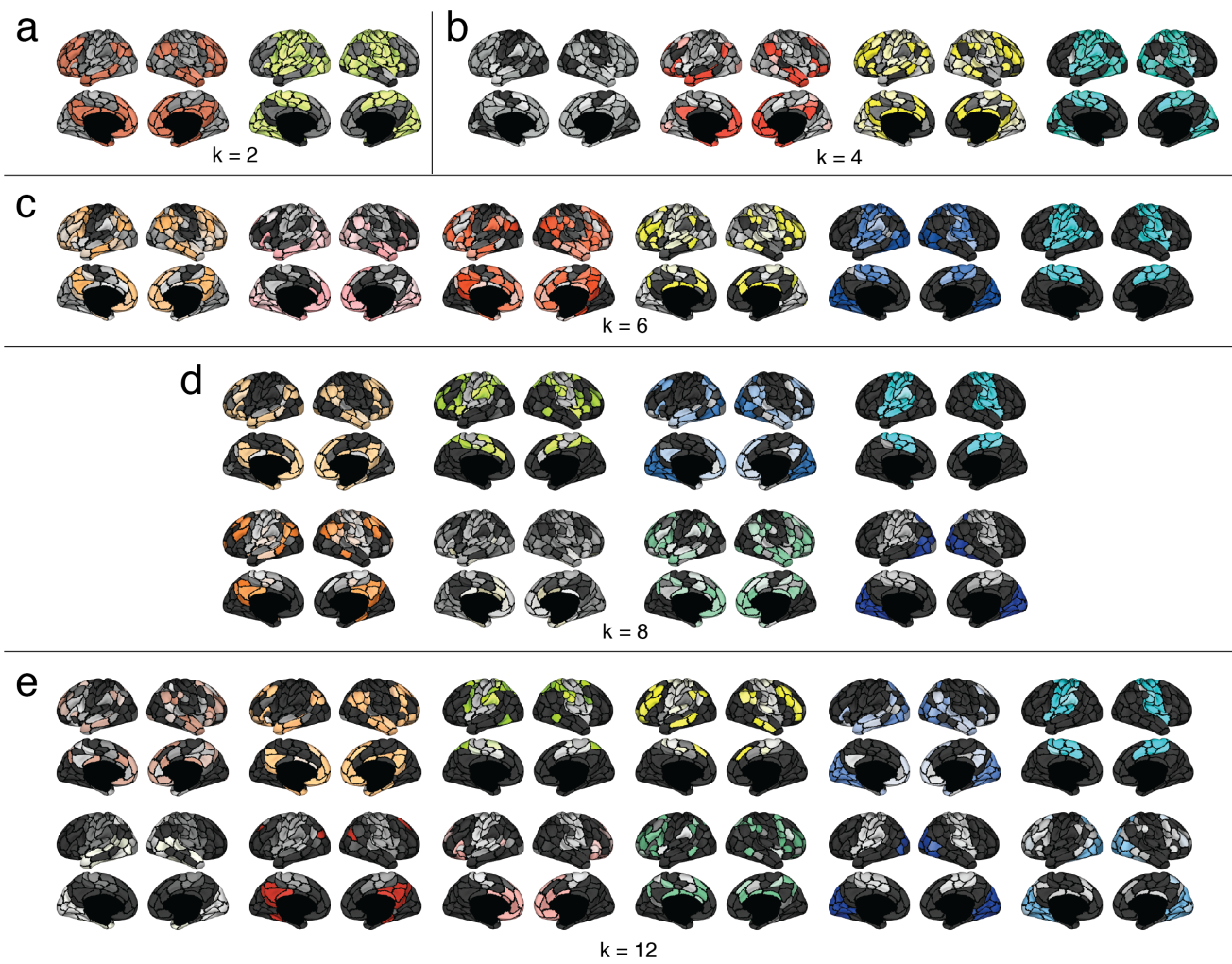
Supplementary Figure 7. Effect of auto-correlation and amount of data on eFC. In the main text we described a procedure for sub-sampling data in which frames were selected to be temporally contiguous, thus approximately preserving the autocorrelation structure found in the original data. Here, we compare this sub-sampling procedure with one in which frames were uniformly and randomly sampled, which does not preserve auto-correlation structure. In general, we find that the random sampling procedure outperforms the one that preserves autocorrelation. For example, in the main text we reported a similarity of $r \approx 0.8$ given a full 30 minutes of scan time. For that same amount of time, the similarity increases to $r \approx 0.9$ when we do not controlling for autocorrelation. Semitransparent, thin lines depict data from individual subjects; Dark, thick lines depict subject-means.



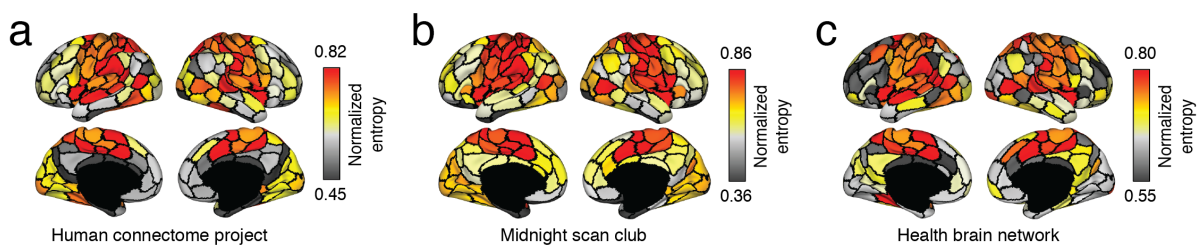
Supplementary Figure 8. Within- versus between-subject similarity of eFC in HBN and HCP datasets. In the main text we showed, using data from the Midnight Scan Club, that eFC was more similar within subjects than between subjects. Here, we show analogous plots for the other two datasets: the Health Brain Network Serial Scanning Initiative and the Human Connectome Project. Panel *a* shows between- and within-subject similarity for the HBN dataset. Panels *b* and *c* depict an analogous figure for HCP data. Panel *b* calculates between- and within-subject similarity treating all four scans (REST1_LR, REST1_RL, REST2_LR, and REST2_RL) independently, whereas panel *c* shows similarity measures for combined REST1_LR + REST1_RL and REST2_LR + REST2_RL. Note that in all cases, the differences of between- and within-subjects similarity were statistically significant (two-sample *t*-tests; all $p < 10^{-15}$; $t_{HBN}(7138) = 46.4$; $t_{HCP4}(79798) = 35.4$; $t_{HCP2}(19898) = 17.74$). In panels *a*, *b*, and *c*, the total number of within-subject samples were $n_w^{HBN} = 647$, $n_w^{HCP4} = 600$, $n_w^{HCP2} = 100$, respectively. The total number of between subject samples were $n_b^{HBN} = 6493$, $n_b^{HCP4} = 79200$, $n_b^{HCP2} = 19800$, respectively. Boxplots, shown in green and overlaid on data points in all panels, depict the interquartile range (box) and median value of the distribution. Whiskers extend to the nearest points $\pm 1.5 \times \text{IQR}$ above and below 25th and 75th percentiles.



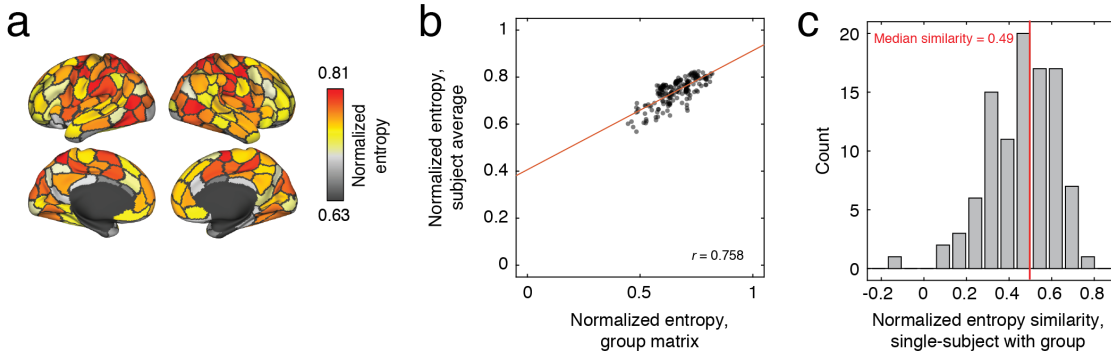
Supplementary Figure 9. Co-assignment probability at different values of k . In the main text we showed the matrix of co-assignment probabilities. In that figure, we reordered the rows and columns to highlight communities detected with $k = 10$. To do so, we truncated the upper limit on the co-assignment probability matrix to correspond with the $k = 10$ communities. Here, we show the same matrix with $k = 2$, $k = 4$, $k = 6$, $k = 8$, and $k = 12$ and without a truncated upper limit.



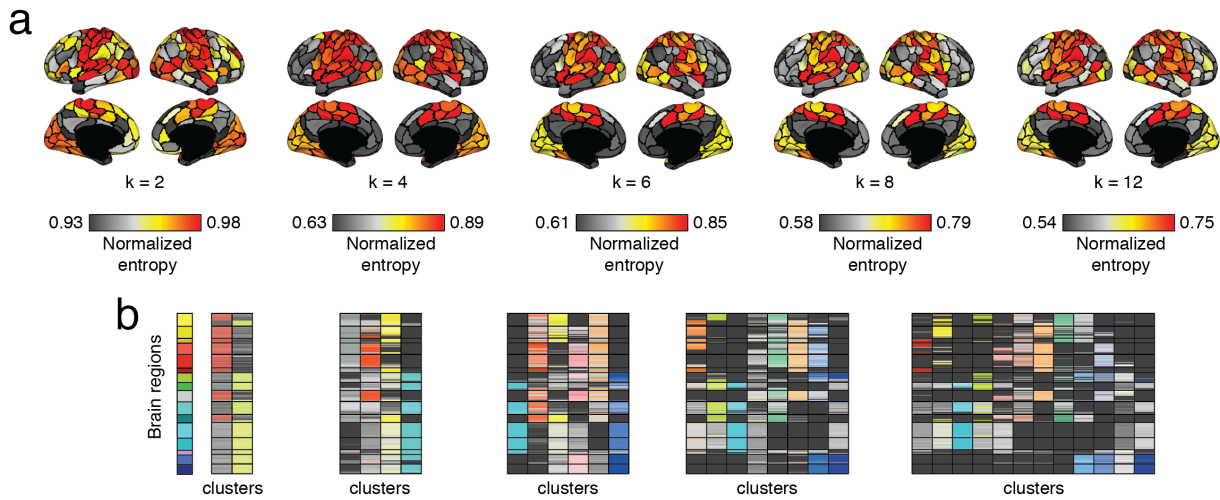
Supplementary Figure 10. Effect of varying k on cluster structure. In the main text we detected clusters when the number of clusters was fixed at $k = 10$. Here, we show examples of clusters detected when $k = 2, k = 4, k = 6, k = 8$, and $k = 12$.



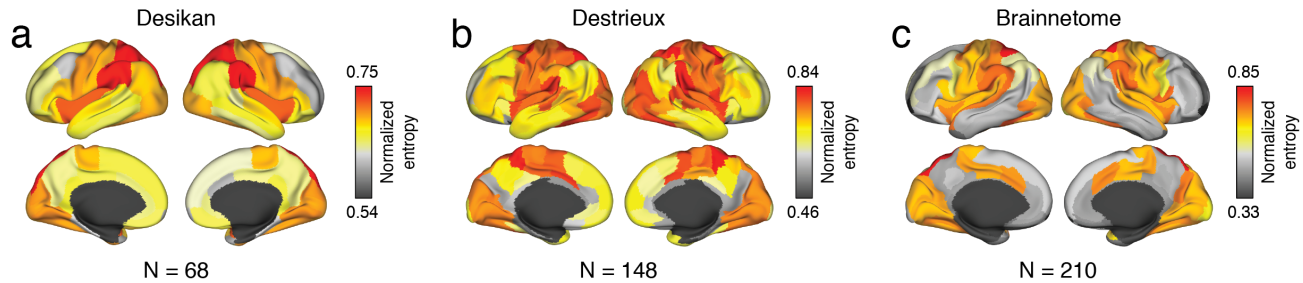
Supplementary Figure 11. Comparison of normalized entropy across datasets. In the main text, we showed the normalized entropy – a measure of cluster overlap – for the HCP dataset. Here, we show the same measure for all three datasets. All plots correspond to $k = 10$ clusters.



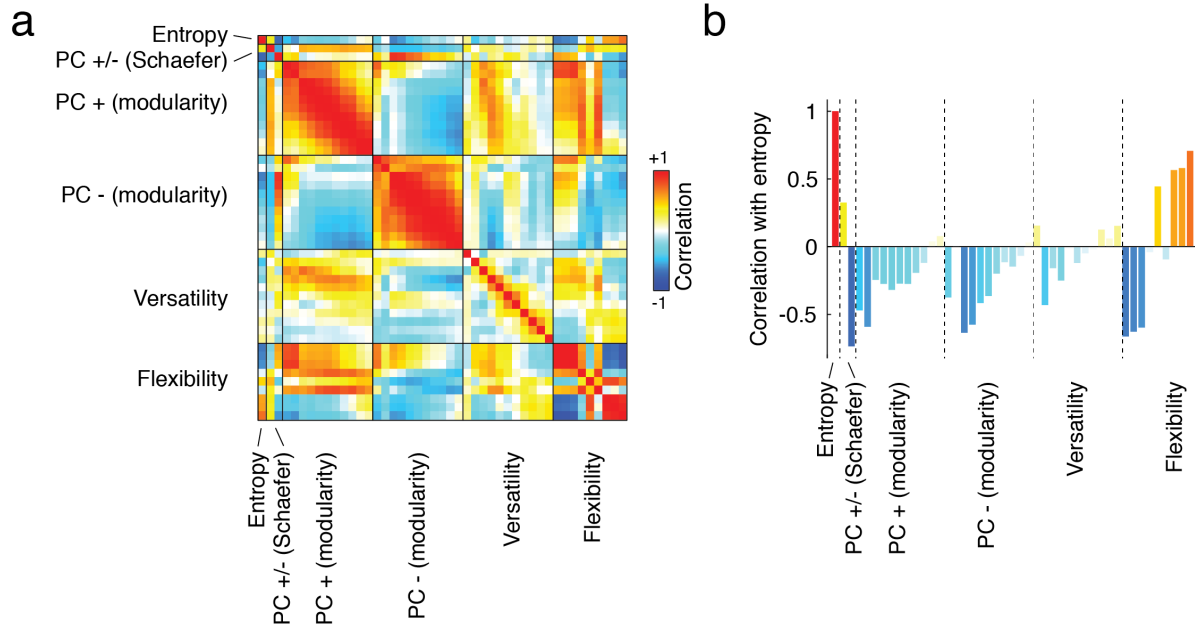
Supplementary Figure 12. Comparison of normalized entropy from group-averaged data with single-subject data. In the main text, we showed the normalized entropy – a measure of cluster overlap – for the HCP dataset estimated by clustering a group-averaged eFC matrix that had undergone a dimension reduction step. Here, we show the similarity of that entropy pattern with entropies obtained from complete (i.e. no dimension reduction) single-subject data from the HCP dataset. (a) Mean normalized entropy pattern after averaging subject-level entropies. (b) Scatterplot showing the relationship of the subject average normalized entropy with the group-representative normalized entropy estimated in the main text ; $n = 200$ entropy values. (c) Correlation coefficients (similarity) of single-subject entropies with the group-representative pattern described in the main text. The median similarity across all subjects was a correlation of $r = 0.49$.



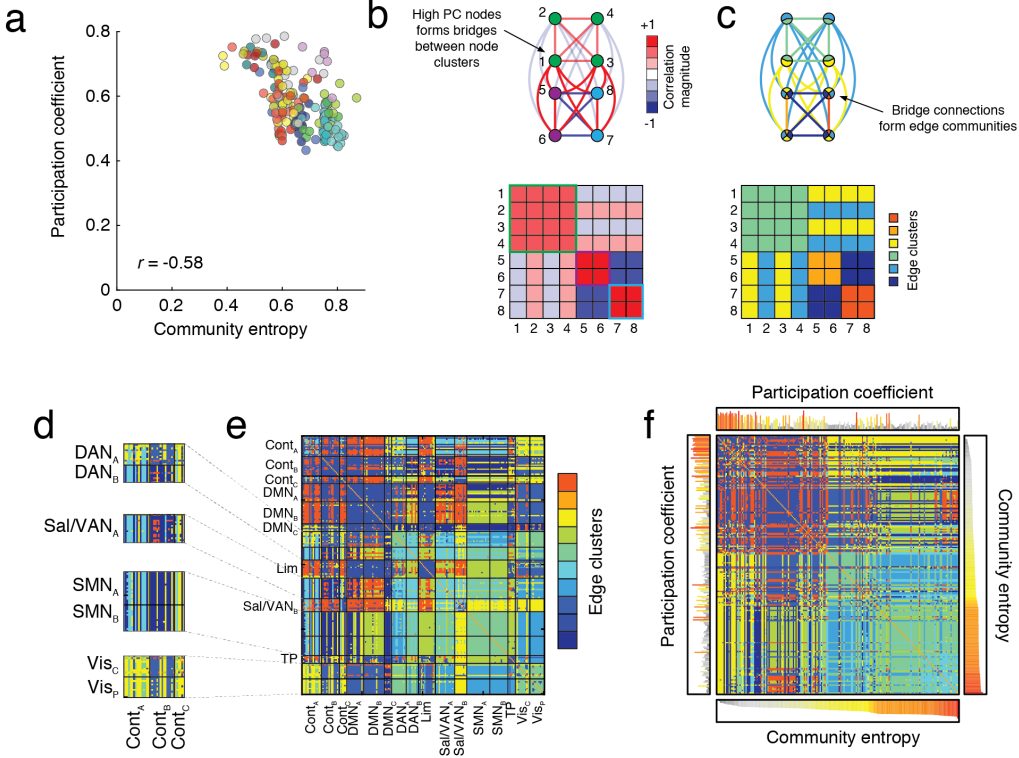
Supplementary Figure 13. Effect of varying k on cluster overlap. In the main text, we showed normalized entropy with the number of clusters fixed at $k = 10$. In panel *a*, we show the same metric as we vary the number of clusters from $k = 2$, $k = 4$, $k = 6$, $k = 8$, and $k = 12$. Panel *b* shows matrix representations of the cluster assignments used to estimate normalized entropy.



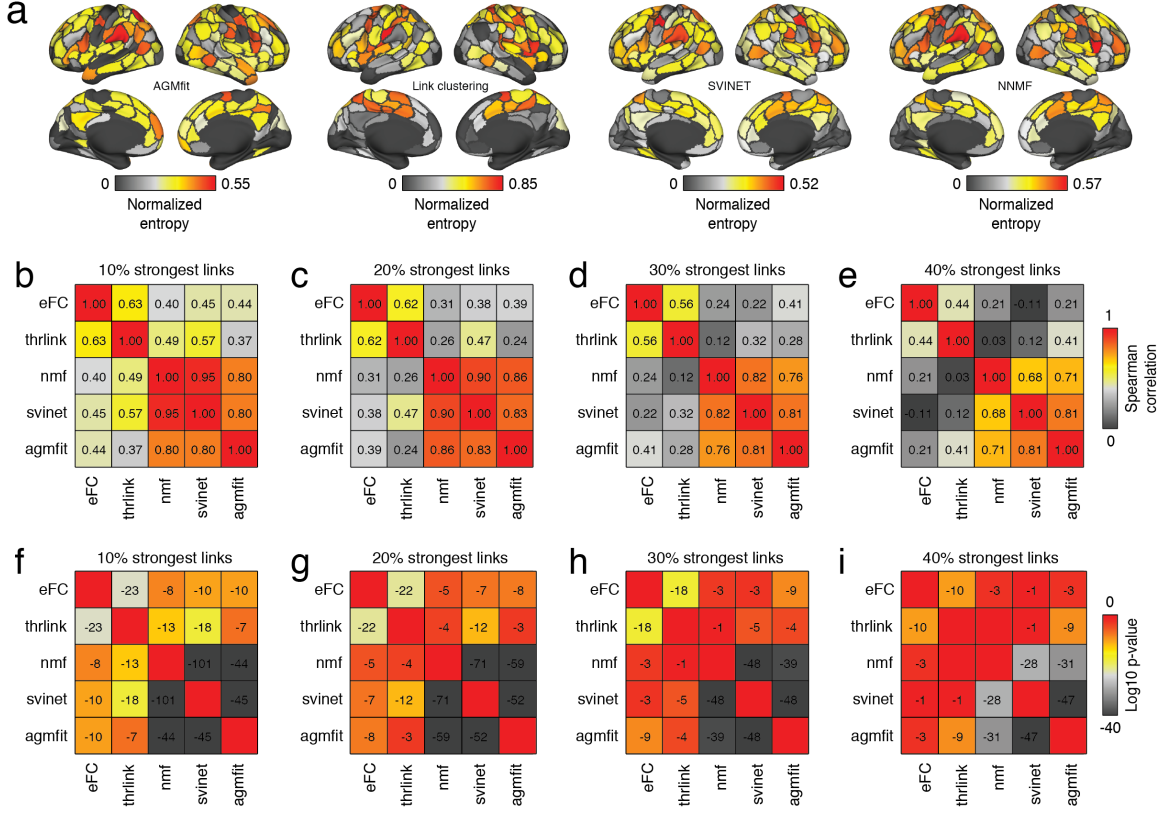
Supplementary Figure 14. Effect of parcellation on community overlap. In the main text we assessed the extent to which a brain region's edges are affiliated with multiple communities. Those analyses were carried out using a parcellation of the brain into $N = 200$ similarly sized and functionally defined regions . Here, we assess the impact of parcellation on measures of overlap. Specifically, we repeated our analysis using two anatomical atlases (Desikan¹ and Destrieux²), which partition the cerebral cortex into $N = 68$ and $N = 148$ regions respectively and a functional parcellation (Brainnetome³) of the brain into $N = 210$ nodes . To establish a correspondence between eFC generated from these atlases, we projected normalized entropy values to surface vertices for the three above-mentioned atlases and calculated the spatial correlation (Spearman correlation) with an analogous projection of the entropy map described in the main text. In general, we found that there was a strong correspondence across atlases. The strongest correlation involved the Brainnetome atlas ($\rho = 0.74$, $p < 10^{-15}$), which was most similar to the data described in the main text in terms of number of parcels and the fact that parcels were functionally defined. The other two atlases exhibited significant but slightly weaker correspondences with the data in the main text ($\rho = 0.47$ and $\rho = 0.55$ for the Desikan and Destrieux atlases, respectively; both $p < 10^{-15}$). ¹Desikan, R. S. et al. An automated labeling system for subdividing the human cerebral cortex on MRI scans into gyral based regions of interest. Neuroimage 31, 968-980 (2006). ²Destrieux, C., Fischl, B., Dale, A. & Halgren, E. Automatic parcellation of human cortical gyri and sulci using standard anatomical nomenclature. Neuroimage 53, 1-15 (2010). ³Fan, L. et al. The human brainnetome atlas: a new brain atlas based on connectional architecture. Cerebral cortex 26, 3508-3526 (2016).



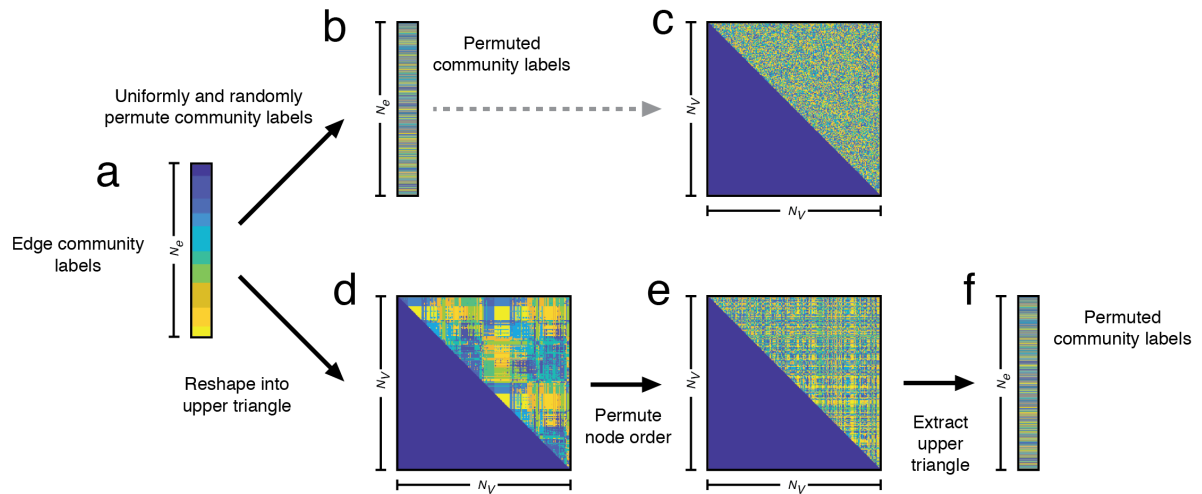
Supplementary Figure 15. Correspondence of overlap (node entropy) with existing measures of overlap. In the main text we propose an overlap metric that assesses the uniformity with which a node's edges are assigned to communities. This metric is largest when edges are assigned uniformly and smallest when they are assigned to a small number of communities. Here, we compare that entropy measure with existing measures of overlap. Specifically, we compare node entropy (with the number of communities fixed at $k = 10$ as in the main text) with signed participation coefficients estimated with respect to the system labels and partitions detected using modularity maximization with a uniform null connectivity model while varying the structural resolution parameter, γ , over 11 values linearly-spaced between the interval $[0, 0.5]$. We also estimated nodal versatility at each resolution using multi-layer modularity maximization at all nine parameter combinations of $\gamma = [0, 0.25, 0.5]$ and $\omega = [0.1, 0.5, 1]$. In general, we found that the node entropy score was not well approximated by participation coefficient or versatility. Flexibility estimated with $\gamma = 0.5$ achieved the greatest correspondence ($r = 0.71$) but also resulted in partitions where the average number of communities per layer was equal to 67.2 ± 4.4 (or ≈ 3 nodes per community). (a) The full correlation matrix of all measures. (b) The first column/row depicting correspondence of node entropy with the other measures.



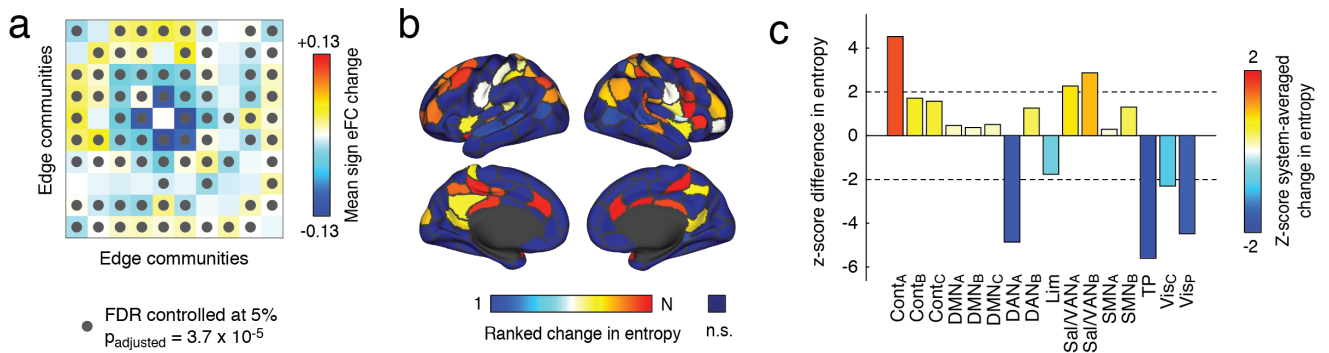
Supplementary Figure 16. Overlap from node- and edge-centric perspectives. In the main text we cluster eFC and map edge communities back to nodes, revealing overlapping community structure. We find that overlap is greatest in sensorimotor and attentional networks and the lowest in association cortex. This observation, however, conflicts with measures of overlap derived from nFC, which report the opposite pattern. Here, we explore the origins of this conflict. (a) We first calculated a modified version of participation coefficient (PC), an overlap measure commonly applied to nFC, that takes into account the weights and signs of connections. Specifically, we generated a fully weighted and signed composite nFC matrix (HCP dataset; all subjects and all scans) and used modularity maximization to detect its community structure. Modularity maximization requires the user to specify a “resolution parameter” that determines the number and size of communities. We selected a value that, after experimentation, resulted in 10 communities on average, matching the number of edge clusters reported in the main text. As expected, we found that PC and the community entropy metric described in the main text are anti-correlated. Why is this? The explanation has to do with differences in how nFC and eFC handle edges that fall between node clusters. Consider a node that makes strong connections to its own module, but also less strong connections to another module (or modules). See, for example, the node highlighted in panel b. The PC of this “bridge node” would be relatively large, rightly indicating that it has strong affiliations with multiple modules. This same scenario plays out differently under the edge-centric approach. In this example, the bridge node’s between-module connections can be clustered separately, forming their own community (labeled yellow in panel c). This community involves many edges, all of which have the bridge node in common. From the bridge node’s perspective, the fact that lots of its edges belong to the same community reduces its entropy (lower overlap). The opposite is true from the perspective of the other nodes in the community; their participation increases the variety of communities they participate in, leading to increased entropy (greater overlap). When edge communities are mapped into a node-by-node matrix (panel c, bottom) this mechanism (high participation to low entropy via adopting an edge-centric representation) leads to distinctive pattern of “bands”. Note the yellow and cyan bands in panel c, bottom). Interestingly, we see precisely the same patterns in empirical data. (d) We show edge community assignments of nodes in the three sub-components of the control network with other nodes in dorsal attention, salience/ventral attention, somatomotor, and visual networks. Notice that in all cases “banding” is oriented in line with the control network nodes (vertical bands, in this case), ensuring that the control network nodes will have reduced entropy while nodes in the other systems will have increased entropy. For completeness, we show the full matrix of edge communities ordered by system (e) and by node entropy (f). Note that in the margins of panel f we show node entropy and PC in the same order as the rows and columns of the matrix.



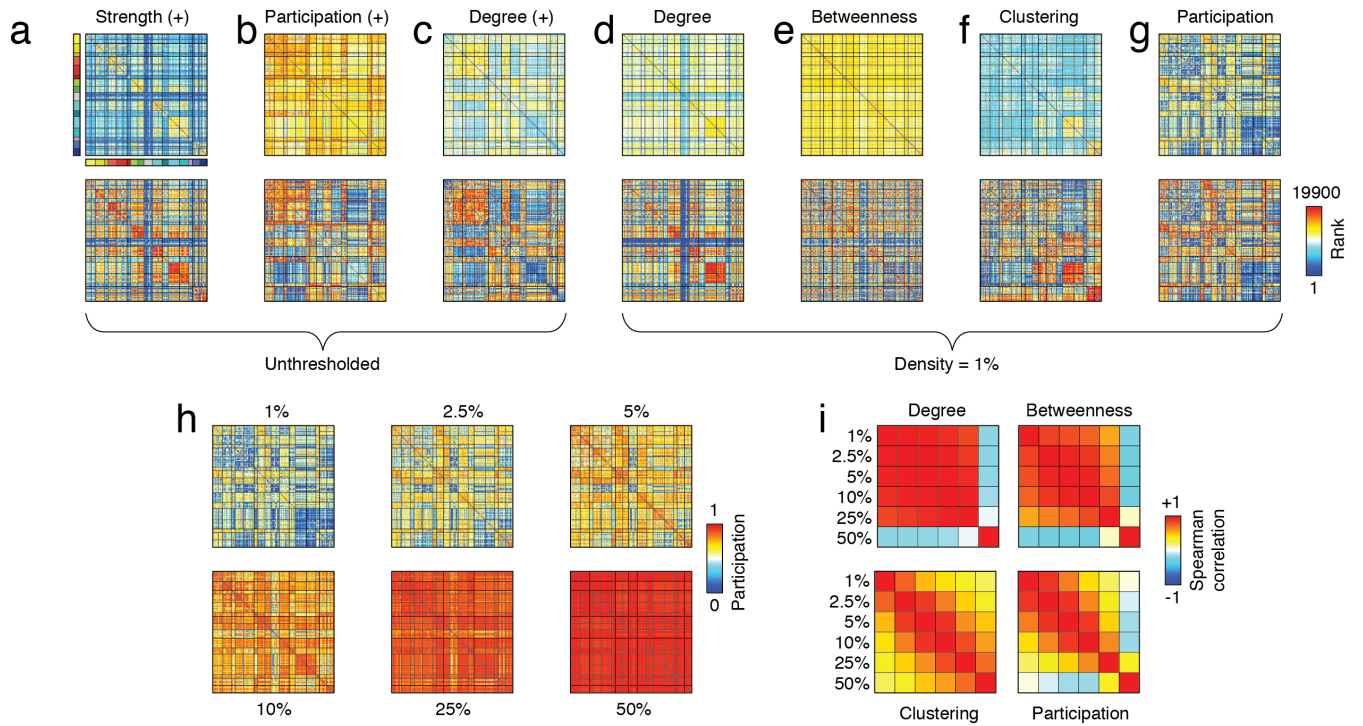
Supplementary Figure 17. Comparison of normalized entropy between overlap methods. In the main text we described overlapping communities obtained by clustering eFC. Here, we compare those communities in terms of their overlap with four alternative methods for obtaining overlapping community structure on the nFC matrix: stochastic variational inference for the mixed-membership stochastic block model (*SVINET*), the Affiliation Graph Model (*AGMfit*), Bayesian non-negative matrix factorization (*NMF*), and thresholded weighted link clustering (*ThrLink*). For each method we estimated community structure 250 times and, for each estimate, calculated the corresponding pattern of normalized entropy. As in the main text, we report the average entropy pattern across the 250 runs. The alternative methods employed could not operate on fully weighted and signed connectivity matrices, necessitating that we impose thresholds on their input data. We repeated the procedure over four different network densities (10%, 20%, 30%, and 40% dense). (a) Normalized entropy patterns for the four alternative methods for obtaining overlapping communities. We found that the patterns of normalized entropy varied across methods ($F(4, 995) = 283.47, p < 10^{-15}$) and were qualitatively different from the entropy pattern obtained from eFC. For example, across methods, visual nodes display low normalized entropy relative to the entropy measured using the eFC structure. The correlation of normalized entropy patterns between methods are shown above, at densities of 10% (b), 20% (c), 30% (d), and 40% (e). The overlap pattern produced by the *ThrLink* method is most correlated to the eFC overlap pattern ($p < 10^{-4}$ across density thresholds; bootstrapped difference of means), which is expected, given that the methods are conceptually most similar. In panels f-i we show the \log_{10} of p-values for each of the correlation coefficients reported in panels b-e (all correlations computed using overlap data from $n = 200$ brain regions).



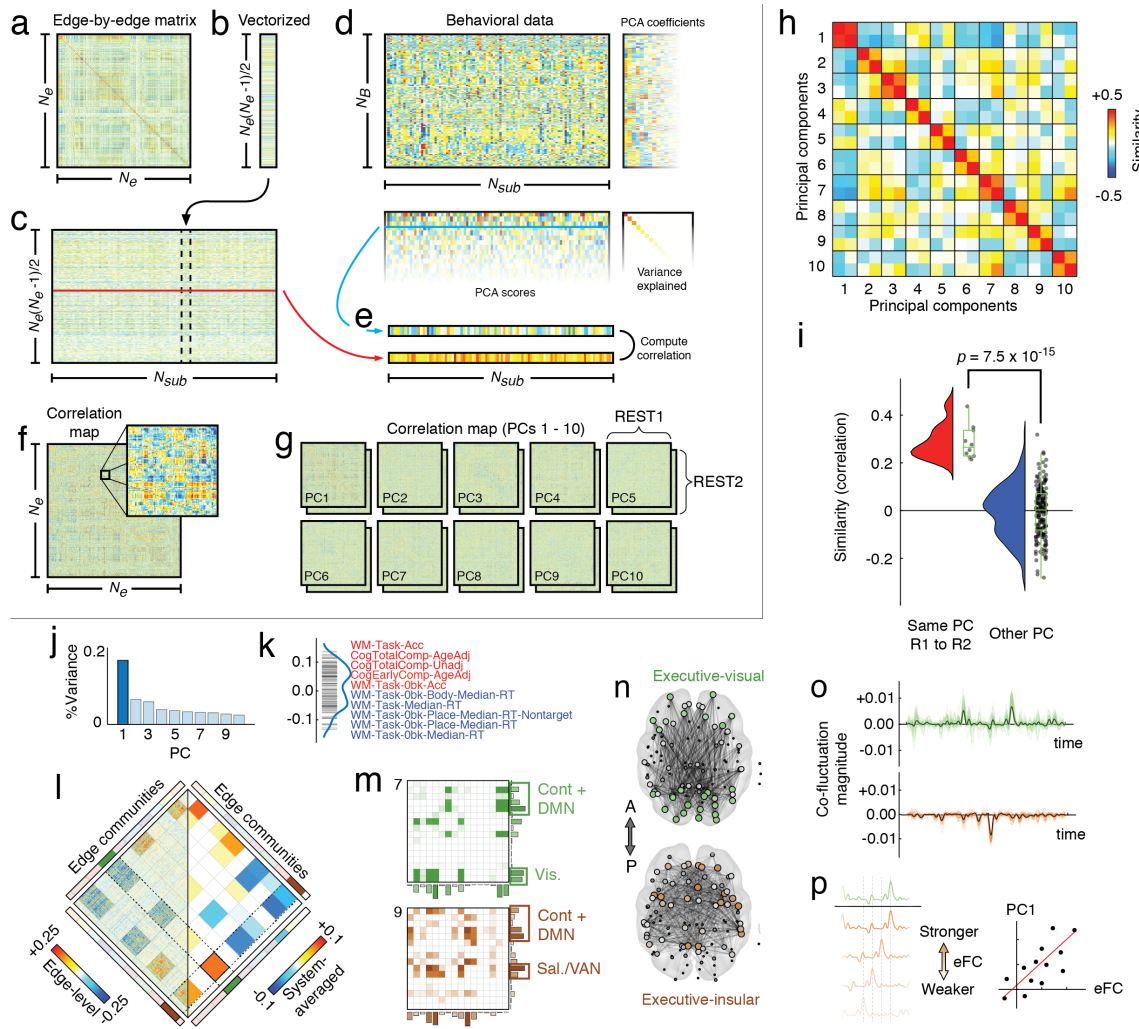
Supplementary Figure 18. Permutation testing procedure for edge community labels. (a) Edge communities can be expressed as a vector of length N_e , where $N_e = N_v(N_v - 1)/2$ is the number of edges in a connectivity matrix of a network with N_v vertices or nodes. There are two strategies for permuting edge labels. (b) The first strategy is to randomly permute the elements in the edge community vector. (c) This procedure, however, does not preserve any relationships among edges, e.g. the fact that many edges involve the same node. (d) A more conservative strategy, on the other hand, involves first reshaping the edge community labels into the upper triangle of a $N_v \times N_v$ matrix, and (e) randomly permuting the rows/columns of this matrix before (f) extracting the permuted elements from the upper triangle. By definition, this second strategy preserves the relationship among a node and its edges, but otherwise randomizes the elements of the edge community labels.



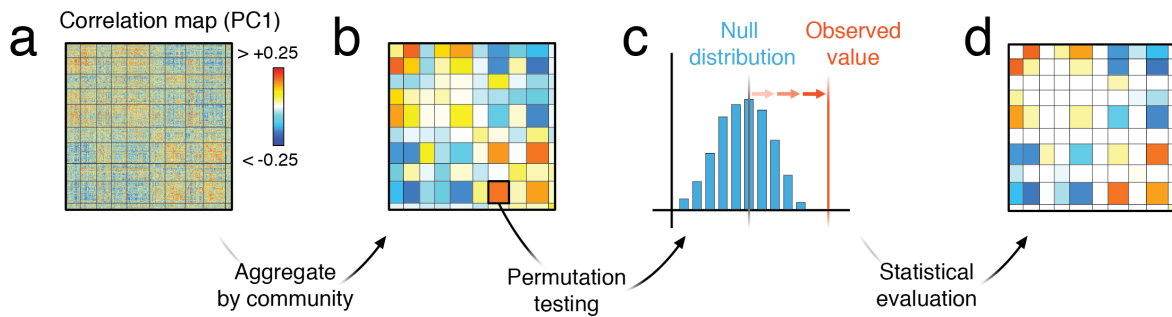
Supplementary Figure 19. Statistical analysis of movie *versus* rest comparisons. In the main text we compared movie-watching and rest in terms of eFC. Here, we show results of additional statistical tests not included in the main text. (a) We tested whether mean within- and between-community eFC differed between movie-watching and rest. Here, we show results after randomly reordering community labels by inserting them into the upper triangle of a node-by-node matrix, randomly permuting its rows and columns, and extracting from the row-/column-permuted matrix its upper triangle elements. Black dots indicate pairs of communities where the inter-condition difference in eFC exceeded what would be expected by chance (multiple comparisons controlled by fixing false discovery rate to 5%; $p_{adjusted} = 3.7 \times 10^{-5}$; two-sample permutation test). (b) In the main text we also compared node entropy – a measure of community overlap – between movie-watching and resting conditions. Here, we show nodes whose difference in overlap exceeded what would be expected had condition labels been randomly permuted. As in the main text, we show differences in terms of rank. We note, however, that all statistical tests were carried out on the raw entropy values. (c) Finally, we tested whether the node-level differences in entropy exhibited system specificity. To test this, we calculated the average change in entropy for each of the 16 cognitive systems and compared the observed chance in entropy with what would be expected had system labels been randomly permuted. Here, we show z-scores of the original entropies; large positive and negative z-scores indicate that the observed differences in entropy were greater than expected by chance.



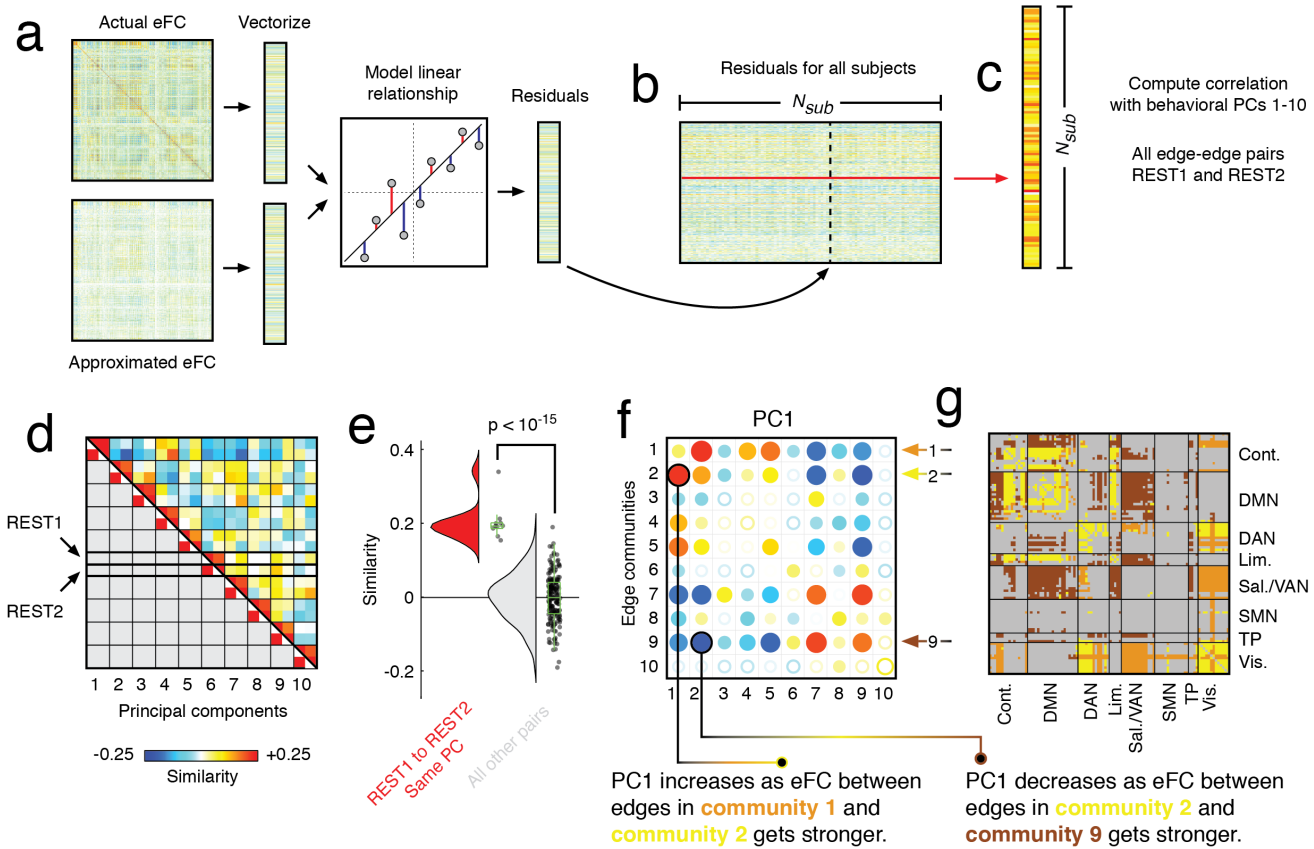
Supplementary Figure 20. Graph-theoretic analysis of eFC matrices. In the main text, we note that eFC can be analyzed using graph theoretic measures in the same way nFC is traditionally analyzed. In panels a-g, we show examples of network graph measures. In all examples, we calculated local metrics that are defined at the level of eFC nodes or nFC edges. To visualize these statistics, we remap the eFC nodes back to the edges of a node-by-node matrix. The top row depicts their raw values; the bottom row depicts values rank transformed, which involved reordering the graph measures in ascending order and assigning each edge a new value equal to the position in which it appeared. Tied values all received the same average rank. (a) Positive strength. (b) Participation coefficient estimated using positive connections only and with respect to consensus partition at $k = 10$. (c) Total number of positive connections incident on each edge in the eFC matrix. (d) Total number of connections incident on each node in the eFC matrix after sparsifying the matrix and retaining only the top 1% connections. (e) Betweenness centrality (log transformed). (f) Clustering coefficient. (g) Participation coefficient estimated with respect to consensus partition at $k = 10$. Note that all in all plots, nodes have been reordered according to cognitive systems. (h) We systematically varied the threshold (1%, 2.5%, 5%, 10%, 25%, and 50%) and recalculated measures at each threshold. Here, we show variation in the participation coefficient across this range. (i) Similarity of graph measures as a function of threshold value.



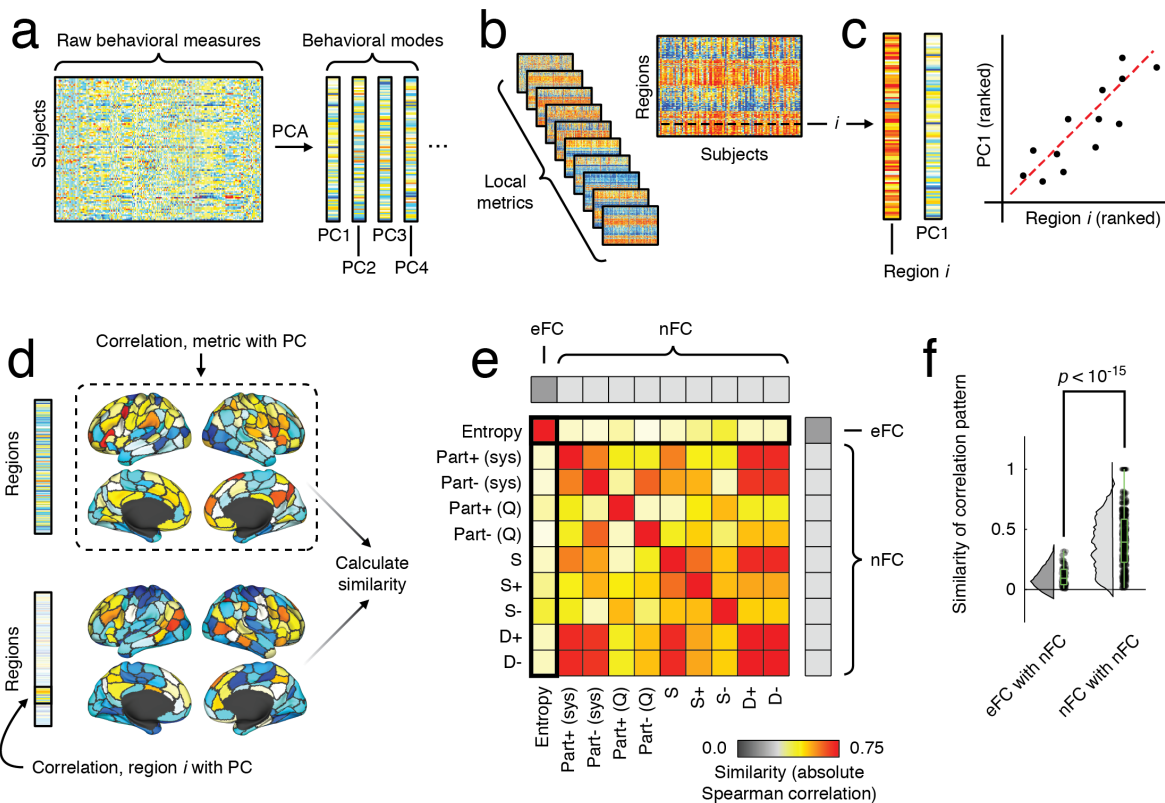
Supplementary Figure 21. Mapping brain-behavior associations using eFC. (a) Each subject's eFC is characterized by an edge-by-edge matrix. (b) We extract the upper triangle elements and represent this matrix as a vector. (c) The set of vectorized eFC from all subjects is stored in a matrix. (d) Concurrently, we z-score the matrix of behavioral data and apply PCA. This results in a set of orthogonal PC scores. (e) We focus on the first 10 PCs and compute the correlation of scores with each row in the matrix of subjects' eFC vectors. (f) This results in a correlation map for each PC. (g) We repeat this analysis separately using eFC calculated using fMRI data from scans REST1 and REST2. (h) We find that correlation maps using the same PC are similar between REST1 and REST2. (i) Statistically, we find higher levels of similarity between REST1 and REST2 using the same PC (two-sample t-test; $t(188) = 8.5$; $p = 7.6 \times 10^{-15}$); $n = 190$ correlation coefficients comparing principal component scores estimated using eFC data from REST1 and REST2 scans. Boxplots, shown in green and overlaid on data points in panel i, depict the interquartile range (box) and median value of the distribution. Whiskers extend to the nearest points $\pm 1.5 \times IQR$ above and below 25th and 75th percentiles.. (j) For the sake of interpretation, we focus on PC1, which explains 17% of total variance and (k) characterizes tradeoffs between accuracy and reaction time. (l) Correlation map of PC1 organized by edge communities. On the left and right sides we show raw and community-averaged edge-edge correlations. Blocks where the community-averaged correlation does not meet statistical significance are presented opaquely (permutation test; false-discovery rate fixed at 5%; $p_{adjusted} = 1.4 \times 10^{-10}$). (m) We further focus on the significant interaction between edge communities 7 (green) and 9 (orange). Community 7 disproportionately involves edges linking the control, default, and visual systems one another, while community 9 involves edges linking control, default, and salience/ventral attention networks. (n) We show these sets of edges in anatomical space. (o) Each edge community corresponds to a group of edges that cohesively fluctuate across time. (p) Thus, as the eFC between communities 7 and 9 becomes stronger, the value of PC1 tends to increase.



Supplementary Figure 22. Schematic illustrating community-level analysis of eFC-behavior correlations. (a) Edge-by-edge correlation map (using first principal component; PC1). Elements in this matrix are correlation coefficients. (b) We then aggregate edge-edge correlations by communities. We highlight here the block between edge communities 7 and 9 (one of the strongest community averaged correlations). This matrix of community-averaged correlations serves as the basis for statistical evaluation. (c) For each community-community block we use a constrained permutation test to assess the likelihood of observing that value had edges been randomly assigned to communities. The observed value of each community-community block is compared against a block-specific null distribution and transformed into a p-value. (d) Using the set of p-values for all blocks, we adjust our statistical threshold by fixing the false discovery rate to a particular value and apply that threshold to each block.



Supplementary Figure 23. Procedure for regressing out the effect of nFC from eFC and estimating brain/behavior associations. (a) For each subject we compute their actual eFC matrix using procedures described in the main text. We also generate an approximation of eFC directly from the nFC matrix (see Fig. 2 in the main text). Both matrices can be vectorized by extracting their upper triangle elements. Then, using linear regression, model the relationship actual and approximated eFC and compute the residual value for each edge-edge connection. (b) We repeat this procedure for all 100 subjects, generating a matrix whose columns correspond to subjects' vectorized residual values. (c) Each row of the matrix has dimensions $[1 \times \#Subjects]$ and encodes the residual value for one edge-edge pair. We relate these rows to behavioral PCs 1-10. This entire procedure is carried out separately for REST1 and REST2, resulting in two sets of correlation maps. (d) Similarity of correlation maps estimated using different PCs and scans. (e) Violin plot of correlation map similarity divided into same PC but different scans (red), and then different PCs and different scans (gray) (two-sample t -test; $t(188) = 9.8$; $p < 10^{-15}$); $n = 190$ correlation coefficients comparing principal component scores estimated using eFC data from REST1 and REST2 scans.. This plot indicates that brain-behavior correlations are stable across scan sessions. Boxplots, shown in green and overlaid on data points, depict the interquartile range (box) and median value of the distribution. Whiskers extend to the nearest points $\pm 1.5 \times \text{IQR}$ above and below 25th and 75th percentiles. (f) eFC-behavior correlation coefficients aggregated by edge communities (with number of communities set to $k = 10$). The color and size of dots indicates the correlation magnitude. Solid dots pass statistical analysis. This community-based representation helps us interpret eFC-behavior correlations. For instance, we find that increased eFC between edges in communities 1 and 2 is accompanied, on average, by increases in PC1. (g) Edges associated with each community are shown in color.



Supplementary Figure 24. Brain-behavior relationships using node-level statistics and comparisons between eFC and nFC. (a) Performing PCA on (z-scored) behavioral measures from the HCP dataset results in a series of behavioral PCs. (b) We derived for each subject a series of node-level statistics from nFC and eFC and (c) computed the correlations of nodal values with each behavioral PC. (d) This procedure resulted in whole-brain correlation maps for each measure, which we compared against one another (absolute Spearman correlation). (e) Similarity matrix for all measures considered. The lone measure derived from eFC is the normalized entropy (*Entropy*) that describes the community overlap for each region. From nFC, we consider four versions of the participation coefficient (based on positive/negative connections and defined with respect to canonical brain systems and communities detected using modularity maximization), node strength (*S*), positive/negative node strength (*S+*, *S-*), and positive/negative node degree (*D+*, *D-*). Each element in the similarity matrix expresses the average pairwise similarity of correlation patterns over the first 10 PCs. (f) We found that, on average, Entropy was dissimilar with respect to the nFC measures (two-sample *t*-test; $t(898) = 17.3$; $p < 10 \times 10^{-15}$). Boxplot depict the interquartile range (box) and median value of the distribution. Whiskers extend to the nearest points $\pm 1.5 \times$ IQR above and below 25th and 75th percentiles. Note, the points in the boxplot represent pairwise similarity values for each of the first 10 PCs without any averaging; $n = 450$ pairwise comparisons of node-level network statistics (45 for each PC, 10 PCs in total). These observations suggest that brain-behavior correlation patterns estimated using measures derived from eFC are different from using measures derived from nFC. Importantly, this analysis controls for the differences in dimensionality between eFC and nFC by focusing on derivative measures of equal dimension.

PC	Name	Top 5	Bottom 5
1	Accuracy-reaction time axis	WM-Task-Acc (0.14) CogTotalComp-AgeAdj (0.14) CogTotalComp-Unadj (0.13) CogEarlyComp-AgeAdj (0.13) WM-Task-0bk-Acc (0.13)	WM-Task-0bk-Body-Median-RT (-0.12) WM-Task-Median-RT (-0.13) WM-Task-0bk-Place-Median-RT-Nontarget (-0.13) WM-Task-0bk-Place-Median-RT (-0.13) WM-Task-0bk-Median-RT (-0.13)
2	Positive-negative affect (axis 1)	FearAffect-Unadj (0.14) WM-Task-2bk-Tool-Median-RT-Nontarget (0.13) WM-Task-2bk-Tool-Median-RT (0.13) WM-Task-2bk-Median-RT (0.13) Sadness-Unadj (0.13)	PMAT24-A-SI (-0.10) Friendship-Unadj (-0.11) EmotSupp-Unadj (-0.11) VSPLIT-OFF (-0.11) PosAffect-Unadj (-0.12)
3	Positive-negative affect (axis 2)	PercStress-Unadj (0.17) Loneliness-Unadj (0.16) NEOFAC-N (0.15) AngHostil-Unadj (0.15) PercReject-Unadj (0.14)	WM-Task-2bk-Tool-Median-RT (-0.12) DDisc-SV-5yr-200 (-0.12) Friendship-Unadj (-0.13) DDisc-SV-1yr-40K (-0.13) LifeSatisf-Unadj (-0.13)
4	Unknown	WM-Task-0bk-Acc (0.18) WM-Task-0bk-Body-Acc-Target (0.18) SCPT-TN (0.16) SCPT-SPEC (0.16) WM-Task-0bk-Body-Acc (0.15)	SCPT-FP (-0.16) Strength-Unadj (-0.16) Strength-AgeAdj (-0.17) Endurance-Unadj (-0.18) Endurance-AgeAdj (-0.18)
5	Executive function and reward (axis 1)	DDisc-SV-6mo-200 (0.17) DDisc-SV-3yr-40K (0.16) DDisc-AUC-40K (0.15) Gambling-Task-Perc-Larger (0.15) DDisc-SV-10yr-40K (0.15)	WM-Task-2bk-Tool-Median-RT (-0.12) Strength-Unadj (-0.13) Strength-AgeAdj (-0.14) Gambling-Task-Reward-Perc-Smaller (-0.14) Gambling-Task-Perc-Smaller (-0.15)
6	Executive function and reward (axis 2)	Gambling-Task-Reward-Perc-Larger (0.21) Gambling-Task-Perc-Larger (0.21) Gambling-Task-Punish-Median-RT-Larger (0.16) Gambling-Task-Median-RT-Larger (0.15) Social-Task-Random-Perc-Unsure (0.13)	DDisc-SV-5yr-40K (-0.17) DDisc-SV-3yr-40K (-0.17) DDisc-AUC-40K (-0.17) Gambling-Task-Perc-Smaller (-0.21) Gambling-Task-Reward-Perc-Smaller (-0.21)
7	Social cognition	Social-Task-Perc-Random (0.23) Social-Task-Random-Perc-Random (0.21) PSQI-AmtSleep (0.14) SCPT-LRNR (0.12) ER40-CR (0.12)	PSQI-Score (-0.16) PSQI-Comp3 (-0.17) Social-Task-Random-Perc-TOM (-0.18) PSQI-Comp4 (-0.18) Social-Task-Perc-TOM (-0.21)
8	Generalized cognition and intelligence	WM-Task-2bk-Tool-Acc (0.20) WM-Task-2bk-Tool-Acc-Target (0.19) Flanker-AgeAdj (0.17) Flanker-Unadj (0.17) CogFluidComp-Unadj (0.17)	AngAggr-Unadj (-0.12) ReadEng-Unadj (-0.13) ReadEng-AgeAdj (-0.13) CogCrystalComp-Unadj (-0.14) CogCrystalComp-AgeAdj (-0.14)
9	Unknown	ER40FEAR (0.16) PSQI-Comp4 (0.14) SCPT-LRNR (0.14) Gambling-Task-Punish-Perc-Larger (0.14) PSQI-TooHot (0.13)	Relational-Task-Median-RT (-0.14) WM-Task-2bk-Acc (-0.15) WM-Task-2bk-Tool-Acc (-0.15) Strength-Unadj (-0.16) Strength-AgeAdj (-0.16)
10	So-social/language axis	Social-Task-TOM-Median-RT-TOM (0.21) Social-Task-Median-RT-TOM (0.21) Language-Task-Median-RT (0.21) Language-Task-Story-Median-RT (0.18) VSPLIT-TC (0.16)	Emotion-Task-Shape-Acc (-0.14) VSPLIT-OFF (-0.14) WM-Task-2bk-Body-Median-RT-Nontarget (-0.15) Emotion-Task-Acc (-0.15) PSQI-WakeUp (-0.17)

Supplementary Table I. Description of first 10 behavioral PCs. Rows correspond to specific PCs and show the top and bottom five terms ordered by PC coefficient. Each row also includes a “title” for each PC. For instance, PC1 organizes behavioral measures along an accuracy-reaction time gradient; PC2 and PC3 capture distinct gradients of positive and negative affect, PC5 and PC6 span executive function and reward processing, PC7 and 10 track social cognition and language function, and PC8 tracks general cognition and intelligence. In the cases of PC4 and PC9, we did not observe obvious relationships among the most positive/negative terms. We note that in general, PCs reflect low-dimensional modes of variability within a large set of behavioral measures. While ascribing names to PCs provides readers with intuition about the kind of behaviors that each PC captures, it entails a degree of subjectivity.